Beamspace MIMO Prototype for Low-Complexity Gigabit/s Wireless Communication

John Brady, Paul Thomas, David Virgilio, and Akbar Sayeed
Department of Electrical and Computer Engineering
University of Wisconsin - Madison

***Abstract*—The rapid proliferation of data hungry devices is creating a bandwidth crisis, with aggregate data rates expected to increase 1000 fold by 2020. Millimeter-wave (mm-wave) systems, operating in the 30-300GHz band, are poised to meet this exploding demand through large bandwidths and high-dimensional MIMO operation. However traditional MIMO techniques result in prohibitively high-complexity transceivers. In this paper, we report initial results on a Continuous Aperture Phase MIMO (CAP-MIMO) prototype that uses a discrete lens array (DLA) for analog spatial beamforming to reduce complexity. The CAP-MIMO prototype is based on the theory of beamspace MIMO communication – modulating data onto orthogonal spatial beams – to achieve near-optimal performance with the lowest transceiver complexity. We build on previous theoretical and experimental results to construct a prototype CAP-MIMO link at 10GHz for line-of-sight communication and for initial proof-of-concept demonstration. The prototype supports four spatial channels with Gigabits/s data rates.**

***Index Terms*—millimeter-wave wireless, Gigabit wireless, high-dimensional MIMO, massive MIMO, beamforming**

I. Introduction

Capacity demands on wireless networks are growing exponentially due to the mass proliferation of data-hungry devices such as smart phones and tablets. There are numerous communication and signal processing techniques being implemented to address the challenge. One technique uses small cells to leverage spatial reuse as a way of increasing capacity [1]. Another is to use multiple-input multiple-output, MIMO, technology for managing interference and increasing spectral efficiency [2], [3]. Emerging millimeter wave (mm-wave) technology, operating in the 30-300GHz band, is promising in fulfilling the current and future demands on capacity [4].

By moving to mm-wave technology much larger bandwidths become available, in the Gigahertz (GHz) range, compared to current systems which typically utilize tens of MHz of bandwidth. Additionally, the small wavelengths create high-gain, narrow beams, and allow excellent use of the spatial dimension: a given antenna size, A, and wavelength, λ, results in a spatial signal space of dimension $n = \frac{4A}{\lambda^2}$ [5]–[7]. MIMO transceivers can exploit this large spatial signal space dimension for spatial multiplexing to increase spectral efficiency and capacity.

Mm-waves have a highly directional nature, and therefore line-of-sight (LoS) plays a dominant role in propagation. Traditionally MIMO systems have relied on multipath propagation [2], [3], [8], [9]. Due to the narrow beams at mm-wave frequencies, MIMO advantages are possible even in line-of-sight links for both point-to-point (P2P) and point-to-multipoint (P2MP) operation. However, only a small subset $p \ll n$ of the n dimensions make up the spatial communication modes. These p modes are the p beams that couple from the transmitter to the receivers.

Conventional MIMO designs require critically (half-wavelength) spaced antenna arrays to optimally exploit these communication modes via digital beamforming. However, with critical spacing, the number of antennas is on order of n, which, given the short wavelength, can be in the hundreds or thousands. This results in an $\mathcal{O}(n)$ transceiver complexity.

This is the motivation behind the CAP-MIMO transceiver architecture proposed in [5]–[7], based on beamspace MIMO (B-MIMO) theory [9], for efficiently accessing these p spatial communication modes with the lowest transceiver complexity. By using a high resolution discrete lens array (DLA) for analog beamforming, the hybrid analog-digital CAP-MIMO transceiver accesses the p modes with only $\mathcal{O}(p)$ transceiver complexity.

This paper builds on [6], [7], in which CAP-MIMO theory is developed and [5], in which initial measurement results are reported on a DLA-based P2P link. Section II reviews B-MIMO theory and CAP-MIMO architecture. Section III outlines the prototype specifications, construction, and expected performance. Section IV discusses new measurement results, and Section V contains concluding remarks.

Notation: Lowercase boldfaced letters (e.g., $\mathbf{h}$) denote complex-valued column vectors, and uppercase boldfaced letters denote matrices (e.g., $\mathbf{H}$) and $\mathbf{H}^H = (\mathbf{H}^T)^*$ denotes the complex conjugate transpose of $\mathbf{H}$.

II. Beamspace MIMO Theory

This section gives a brief overview of B-MIMO theory. For simplicity, we discuss the theory for 1D systems equipped with linear antennas–extention to 2D planar antennas, as in the prototype, is straightforward [6].

A. Sampled MIMO System Representation

Consider a linear antenna of length L. If the aperture is sampled with critical spacing, $d = \frac{\lambda}{2}$, where λ is the wavelength, there is no loss of information. Conventional

This work is partly supported by the NSF under grant ECCS-1247583, and the Wisconsin Alumni Research Foundation.

MIMO approaches require critically spaced arrays for optimal performance. The sampled points on the aperture are equivalent to a n-dimensional uniform linear array (ULA) of antennas, where $n = \lfloor \frac{2L}{\lambda} \rfloor$ is the maximum number of spatial modes supported by the antenna/ULA and is proportional to its antenna/beamforming gain [6], [7], [9], [10]. A MIMO system with ULAs at the transmitter and the receiver can be modeled as

$$\mathbf{r} = \mathbf{H}\mathbf{x} + \mathbf{w} \tag{1}$$

where $\mathbf{H}$ is the $n_R \times n_T$ aperture domain channel matrix representing coupling between the transmitter and receiver ULA elements, $\mathbf{x}$ is the n_T-dimensional transmitted signal vector, $\mathbf{r}$ is the n_R-dimensional received signal vector, and $\mathbf{w} \sim \mathcal{CN}(\mathbf{0}, \mathbf{I})$ is the n_R-dimensional vector of unit variance additive white Gaussian noise.

B. Beamspace MIMO System Representation

The B-MIMO system representation is obtained from (1) via fixed beamforming at the transmitter and the receiver. Each column of the beamforming matrix, $\mathbf{U}_n$, is an array steering/response vector at a specified angle [6], [7], [9]. For a critically spaced ULA, a plane wave in the direction of angle ϕ corresponds to a spatial frequency, $\theta = 0.5\sin(\phi)$, and the corresponding array steering/response (column) vector and $\mathbf{U}_n$ are given by [9]

$$\mathbf{a}_n(\theta) = \left[e^{-j2\pi\theta i}\right]_{i\in\mathcal{I}(n)}, \ \mathbf{U}_n = \frac{1}{\sqrt{n}}\left[\mathbf{a}_n\left(\Delta\theta_o i\right)\right]_{i\in\mathcal{I}(n)} \tag{2}$$

where $\mathcal{I}(n) = \{i-(n-1)/2 : i = 0, \cdots, n-1\}$ is a symmetric set of indices. The columns of $\mathbf{U}_n$ correspond to n fixed spatial frequencies/angles with uniform spacing $\Delta\theta_o = \frac{1}{n}$, which represent n *orthogonal beams*, with beamwidth $\Delta\theta_o$. These beams cover the entire spatial horizon ($-\pi/2 \le \phi \le \pi/2$) and form a basis for the n-dimensional spatial signal [9]. In fact, $\mathbf{U}_n$ is a unitary discrete Fourier transform (DFT) matrix: $\mathbf{U}_n^H\mathbf{U}_n = \mathbf{U}_n\mathbf{U}_n^H = \mathbf{I}$. The beamspace system representation is obtained from (1) as

$$\mathbf{r}_b = \mathbf{H}_b\mathbf{x}_b + \mathbf{w}_b \quad , \quad \mathbf{H}_b = \mathbf{U}_{n_R}^H\mathbf{H}\mathbf{U}_{n_T} \tag{3}$$

where $\mathbf{x}_b = \mathbf{U}_{n_T}^H\mathbf{x}$, $\mathbf{r}_b = \mathbf{U}_{n_R}^H\mathbf{r}$, and $\mathbf{w}_b = \mathbf{U}_{n_R}^H\mathbf{w}$ are the transmitted, received, and noise signal vectors in beamspace. Since $\mathbf{U}_{n_T}$ and $\mathbf{U}_{n_R}$ are unitary DFT matrices, $\mathbf{H}_b$ is a 2D DFT of $\mathbf{H}$ and thus a completely equivalent representation of $\mathbf{H}$ [6], [7], [9].

The $\mathbf{H}_b$ matrix for our prototype with two dominant eigenvalues is shown in Fig. 1(a). In the CAP-MIMO prototype, illustrated in Fig. 1(b), we realize these unitary DFT matrices with DLAs that perform fixed analog beamforming. Due to the highly directional nature of propagation at mm-wave, LoS propagation is expected to be the dominant mode, with some additional sparse (single-bounce) multipath components possible in urban environments [4], [11], [12]. This leads to the key property of *beamspace channel sparsity*, i.e. $p \ll n$ beams couple between the transmitter and the receiver and capture the communication characteristics of the channel. Sparsity

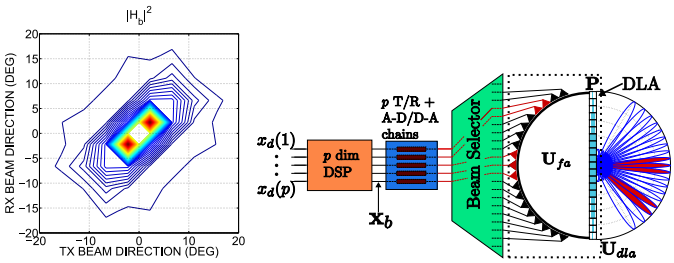

(a) (b)

Fig. 1: (a) Contour plot of $\mathbf{H}_b$ showing its nearly diagonal characteristic. (b) Schematic of CAP-MIMO transceiver showing the p RF chains (blue), beam selector hardware, and DLA which performs analog beamforming.

and DLA-based analog beamforming are exploited to reduce transceiver complexity, from $\mathcal{O}(n)$ (DSP and RF) complexity to $\mathcal{O}(p)$ complexity; see Fig. 1(b). The prototype DLA is $40\text{cm} \times 40\text{cm}$ and designed for a carrier frequency of 10GHz, which results in $n = 26$ (1D). Then $n_T = n_R = 26\times 26 = 676$ (2D), but the number of coupling channels is $p = 2$ for a 1D array, and $p = 4$ for a 2D array [5].

This lower-dimensional beamspace MIMO system can be represented as

$$\tilde{\mathbf{r}}_b = \tilde{\mathbf{H}}_b\tilde{\mathbf{x}}_b + \tilde{\mathbf{w}}_b \tag{4}$$

where the tilde notation ($\tilde{\cdot}$) represents the p-dimensional transmit and receive beamspace signal vectors, and $\tilde{\mathbf{H}}_b$ is the $p \times p$ channel sub-matrix, corresponding to the p beams that couple from the transmitter to the receiver.

C. MMSE Transceiver

The SVD transceiver is the optimal communication architecture [3], [6], [12]. The singular vectors of $\tilde{\mathbf{H}}_b$ are used at the transmitter and receiver to create p non-interfering parallel channels. Waterfilling is used for optimal power allocation across the different spatial channels to achieve capacity. However, the SVD transceiver requires channel state information (CSI) at both the receiver and transmitter, making it impractical in many situations. The minimum mean squared error (MMSE) transceiver transmits independent data streams of equal power on different beams, $E[\tilde{\mathbf{x}}_b\tilde{\mathbf{x}}_b^H] = \rho\mathbf{I}$, where ρ is the SNR per stream, and uses the MMSE estimator at the receiver to suppress interference between different data streams [12]. Unlike the SVD transceiver, the MMSE transceiver only requires CSI at the receiver and is simpler to implement. The MMSE receiver filter is given by [12]

$$\tilde{\mathbf{F}}_{\text{MMSE}} = \arg\min_{\mathbf{F}} E\left[\|\mathbf{F}^H\tilde{\mathbf{r}}_b - \tilde{\mathbf{x}}_b\|^2\right] \tag{5}$$

$$\mathbf{F}_{\text{MMSE}}^H = \tilde{\mathbf{H}}_b^H\left(\rho\tilde{\mathbf{H}}_b\tilde{\mathbf{H}}_b^H + \mathbf{I}\right)^{-1}. \tag{6}$$

The MMSE filtered signal is

$$\tilde{\mathbf{z}}_b = \tilde{\mathbf{F}}_b^H\tilde{\mathbf{r}}_b = \tilde{\mathbf{G}}_b\tilde{\mathbf{x}}_b + \tilde{\mathbf{F}}_b^H\tilde{\mathbf{w}}_b \tag{7}$$

from which different symbol streams can be decoded, and $\tilde{\mathbf{G}}_b = \tilde{\mathbf{F}}_b^H\tilde{\mathbf{H}}_b$.

III. Prototype Design

A. Prototype Specifications

Our initial prototype has a carrier frequency $f_c = 10$ GHz. The DLA is 40 cm$\times$40 cm which results in a spatial dimension $n = 26 \times 26 = 676$. The dimension of the dominant communication subspace for a line-of-sight setup is $p = 4$ [5]. The link length between the two DLAs is $R = 2.67$ m; see Fig. 2(a). The digital-to-analog converters (DACs) and analog-to-digital converters (ADCs) have a symbol/sample rate of 125 MS/s, resulting in a two-sided bandwidth $W = 125$MHz. The DACs use a raised cosine pulse with a roll-off factor of 0.2 and have a maximum output power of 8.5 dBm. All the RF components have a two-sided bandwidth of at least 1GHz.

B. Prototype Construction

The components of the prototype are configured as in Fig. 2(b). For the sake of illustration, only one RF chain is shown, but the FPGAs and oscillators (LO) support up to four RF chains (IQM to WG). The digital inputs and outputs of the DAC and ADC are connected to the FPGA boards by High Speed Mezzanine Card (HSMC) connectors and the analog inputs and outputs are connected to the RF components by SMA coaxial cable connectors. The IQ Mixer (IQM) has two mixers and modulates/demodulates I (in-phase) and Q (quadrature-phase) channels. The bandpass filters (BPF) have a passband from 9.5 to 10.5 GHz. The power amplifiers (PA) and low-noise amplifiers (LNA) have gains of 15 dB and 25 dB, respectively. The feed antennas for the DLAs are straight sections of WR90 wave guide (WG) and are connected to the amplifiers by a wave-guide-to-SMA adapter. The wave guide antennas broadcast a signal which couples to the DLA. Currently the FPGAs are only configured to send and save data. No processing is done on the FPGAs. We save the data (up to $2^{14} = 16\,384$ samples, which is the limit of the on-chip memory of the FPGA) and offload it onto a PC to do post-processing in MATLAB.

C. Expected Performance

Our prototype has an expected per-channel SNR of 63.3 dB. To avoid compression distortion in the IQ Mixers, the DAC analog output is limited to 2.55 dBm of power. The net system loss, measured from DAC output to ADC input, is -5.39 dB. A list of the gains and losses of each component in the prototype is given in Table I. The signal power at the ADC input is -2.84 dBm, that factors in the net system loss of -5.39 dB. There are two primary sources of noise in the system: thermal noise and ADC noise. Thermal noise is calculated by $P_N = 2kTW = -81$ dBm, where k is Boltzmann's constant, $T = 300K$, $W = 1$GHz, and the 2 accounts for noise power in both the I and Q channels. The ADC data sheet lists the noise power as 72.7 dB below the full-scale input power. In our ADC configuration the full-scale input power is 3.5 dBm, giving a noise power of -69.2 dBm per channel (we double to account for noise in the I and Q channels) resulting in ADC noise of -66.2 dBm. If we add the thermal noise power and the ADC noise power we get a total noise power of -66.1 dBm. With this noise power we get an SNR of $2.55 - 5.39 - (-66.1) = 63.3$ dB.

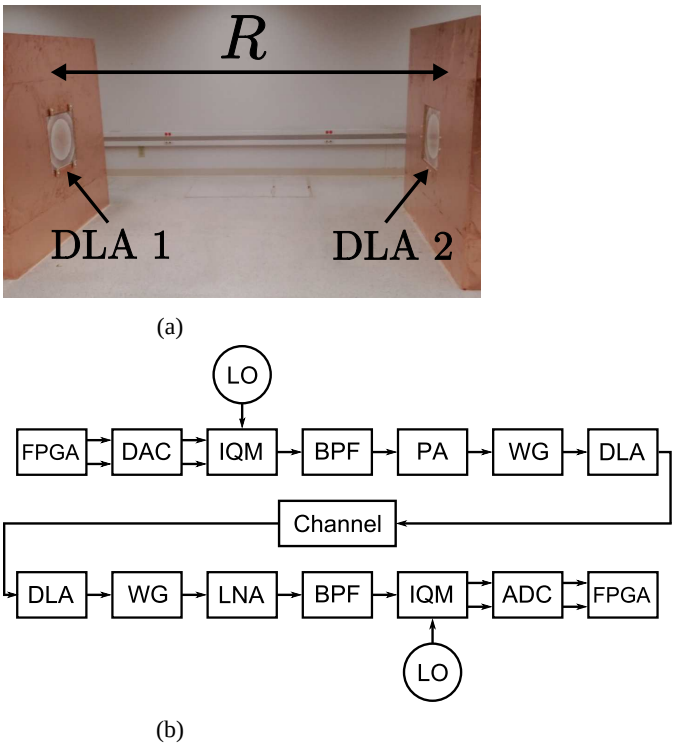

Fig. 2: (a) A picture of the prototype DLA-based lin. (b) Block diagram of one RF chain of the prototype.

Transmitter		Receiver	
Component	Gain (dB)	Component	Gain (dB)
IQM	-7.5	DLA Gain	+29.4
BPF	-0.25	WG-DLA	-6.58
PA	+15	25-ft Cable	-10.5
5-ft cable	-2.5	LNA	+24.0
WG-DLA [5]	-6.58	BPF	-0.54
DLA Gain	+29.4	IQM	-7.5
Channel	-61		
Net System Loss from DAC to ADC:			-5.39 dB

TABLE I: The gains and losses of each component in the prototype from the DAC output to the ADC input. WG-DLA denotes the power loss due to coupling between the feed antenna and DLA. DLA gain denotes the aperture antenna gain.

IV. Experimental Results

All measurements were made in a synchronized system: the transmitter and receiver RF hardware was driven by the same oscillator and the DACs and ADCs shared a reference clock for timing synchronization. The data transmitted was randomly generated QPSK symbols. Unless otherwise specified, data is sent at 125 MS/s.

A. Single Channel System

We start by presenting results for a single transmit and receive chain (as in Figure 2(b)). We present signal captures at three points in the system: the baseband analog I and Q channel output of the DACs (Figures 3(a) and 3(b)); the

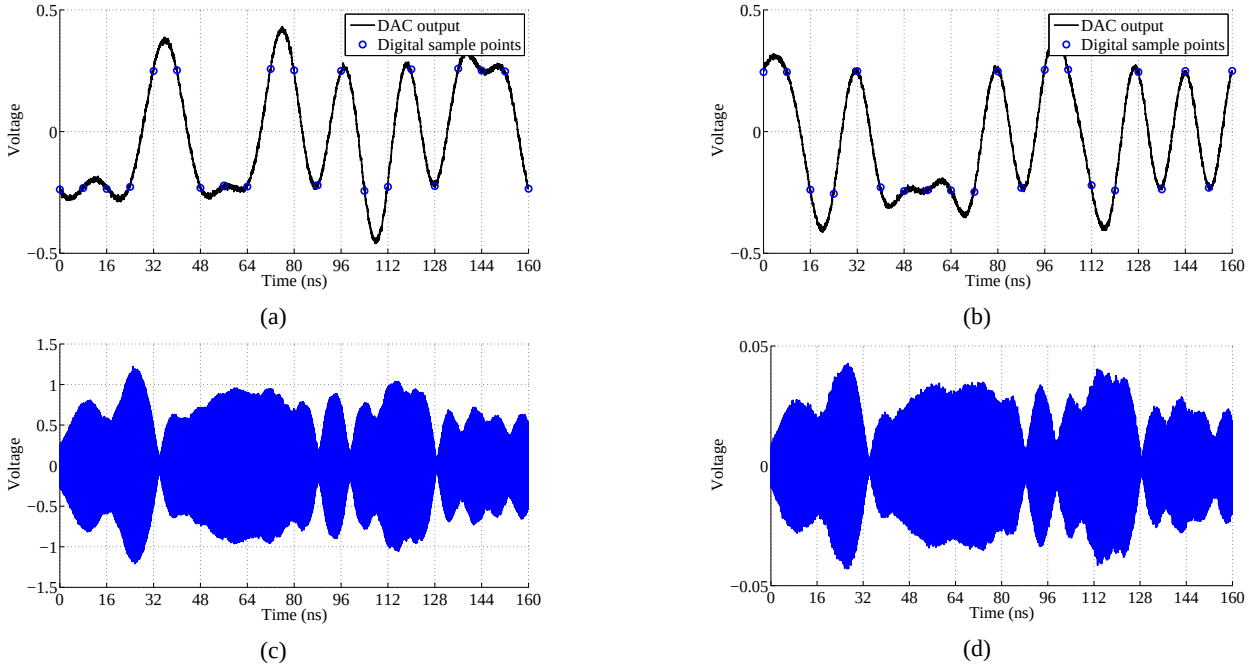

Fig. 3: Signal trace through prototype system. (a) DAC I-channel baseband output. (b) DAC Q-channel baseband output. (c) Passband output of the power amplifier. (d) Passband input to the low-noise amplifier at the receiver.

passband output of the PA (Figure 3(c)); and at the passband input of the LNA (Figure 3(d)). The captures follow the same symbols through the system and were made by an Agilent DSAX93204A Oscilloscope, with 80 GS/s sampling rate and 33 GHz of analog bandwidth.

The recorded signals shown in Figure 4(a) are for an entire block of $16\,384$ (2^{14}) normalized, received QPSK symbols. The spread of the received signals is very large compared to what we expect from the SNR estimation in Section III.C; the majority of this "noise" is due to inter-symbol interference (ISI). To support this claim we captured data with guard intervals of 255 symbols between symbols, shown in Figure 4(b). By calculating the variance of the spread of each received symbol we get a noise power -65 dBm, which is only 1 dB above what we expected. The ISI is due to a non-flat overall frequency response, shown in Figure 4(c). The DACs and ADCs are AC coupled, having a transformer network between the output pins on the chips and the SMA connectors that blocks low frequencies, roughly anything under 250 kHz. This low-frequency blocking can be seen in Figure 4(c). To show how significant the AC coupling is we removed the RF hardware and connected the SMA outputs of the DAC to the SMA inputs of the ADC, shown in Figure 4(d). The spread of received signals is still large, indicating ISI is mainly due to the AC coupling in the DACs and ADCs, with the remaining interference due to RF part of the system.

B. 2×2 *MIMO System*

After verifying single channel operation we configured a 2×2 MIMO system with two transmit and two receive QPSK channels. Our aim is to demonstrate the spatial multiplexing capabilities of CAP-MIMO and the analog beamforming of the DLA. In Fig. 5(a), we show the raw received signal of one channel at full rate. Both ISI and inter-channel interference (ICI) are present. In order to highlight the ICI we added guard intervals of 32 symbol lengths between transmitted symbols to reduce ISI; see Figure 5(b). By applying the MMSE filter at the receiver to the full-rate signal we are able to remove the ICI, as shown in Fig. 5(c); all four symbols are clearly distinguishable and there are no errors. ICI is removed and the remaining ISI is comparable to the ISI in Fig. 4(a). Fig. 5(d) shows the MMSE filtered data for the guard interval data in Fig. 5(b).

The measured channel matrix $\tilde{\mathbf{H}}_b$, the MMSE filter matrix $\tilde{\mathbf{F}}_b$ and the composite channel matrix $\tilde{\mathbf{G}}_b$ matrix from (7) are:

$$\tilde{\mathbf{G}}_b = \tilde{\mathbf{F}}_b^H \tilde{\mathbf{H}}_b = \begin{bmatrix} 1.04\angle 1.5^\circ & 0.003\angle -66.6^\circ \\ 0.001\angle -167^\circ & 1.09\angle -2.8^\circ \end{bmatrix}$$

$$\tilde{\mathbf{F}}_b^H = \begin{bmatrix} 1.19\angle 28.5^\circ & 0.37\angle -21.5^\circ \\ 0.47\angle 5.4^\circ & 1.05\angle -104^\circ \end{bmatrix}$$

$$\tilde{\mathbf{H}}_b = \begin{bmatrix} 0.93\angle -19.7^\circ & 0.34\angle -121^\circ \\ 0.41\angle -90^\circ & 1.10\angle 108^\circ \end{bmatrix}$$

The eigenvalues of $\tilde{\mathbf{G}}_b^H \tilde{\mathbf{G}}_b$ are 1.08 and 1.18 indicating there are two dominant channels. The eigenvalues of $\tilde{\mathbf{H}}_b^H \tilde{\mathbf{H}}_b$ are 0.49 and 1.88.

V. Discussion and Conclusions

There are several non-idealities in the prototype that deserve special attention moving forward on refinement of the current prototype as well as next generation prototypes. First is the significant ISI issue shown in Section IV. The AC coupling in the DACs and ADCs appears to be the primary cause of the ISI in our system; the attenuation of frequencies below 250 kHz.

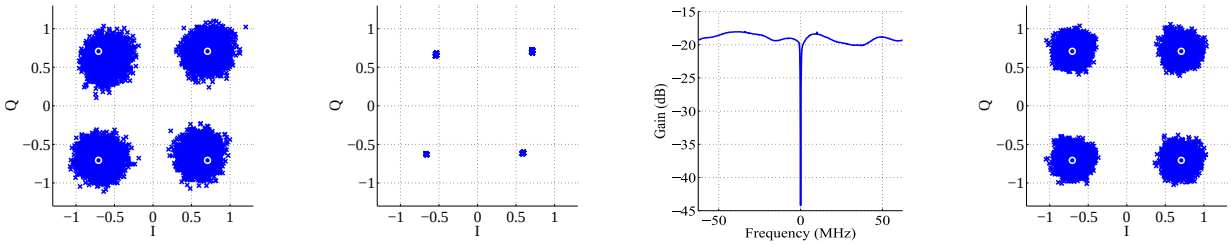

(a) (b) (c) (d)

Fig. 4: (a) Received symbol constellation showing 16 384 QPSK symbols going through entire system at full rate, showing ISI due to baseband and passband components. (b) Received symbol constellation going through entire system with guard intervals between transmitted symbols to eliminate ISI. (c) System frequency response, measured from DAC IC output pin to ADC IC input pin showing the low-frequency distortion due to AC coupling. (d) Received symbol constellation when DAC is directly connected to ADC, showing that ISI is mainly due to AC coupling between DACs and ADCs.

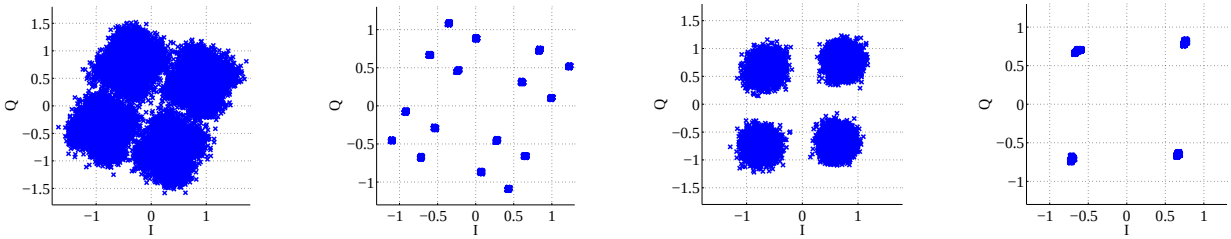

(a) (b) (c) (d)

Fig. 5: (a) Full-rate receive signal of one channel in 2×2 MIMO system showing both ISI and ICI. (b) Receive signal of one channel in 2×2 MIMO system with a guard interval of 32 symbols, highlighting ICI. (c) MMSE filtered full-rate signal of (a). (d) MMSE filtered guard interval signal of (b).

Using DC coupled DACs and ADCs will help eliminate some ISI, additionally, modulation techniques that mitigate ISI, such as OFDM, are being considered. Preliminary simulations using OFDM show promising results.

Synchronization of the transmit and receive local oscillators and sample clocks for the DAC and ADC is another non-ideality we must address. For the results in this paper we eliminated the issue by sharing a single oscillator and sample clock between both the transmitter and receiver. However, in a real system they would necessarily need to be decoupled. For now we have implemented a simple data-directed clock recovery algorithm at the receiver to synchronize the sample clocks [13]. We are still exploring options for local oscillator synchronization. Traditional techniques such as phase-locked loops have been considered, though they add complexity to the system. Modulation schemes that do not depend on oscillator synchronization, such as differential encoding, are also being investigated. Once these issues are addressed the CAP-MIMO link would also provide invaluable channel measurements that are currently unavailable. It is worth noting that a comparable conventional MIMO link, with half-wavelength spaced antennas, would have required antenna arrays with 676 elements!

The results from Sec. IV provide an initial limited proof-of-concept for the CAP-MIMO architecture in terms of beamspace multiplexing in P2P links to deliver multi-Gigabits/s data rates. While these results are promising, additional research and prototype development is needed to demonstrate the full potential of CAP-MIMO in P2MP scenarios via multi-beam steering and data multiplexing.

REFERENCES

[1] V. Chandrasekhar, J. Andrews, and A. Gatherer, "Femtocell networks: A survey," *IEEE Comm. Mag.*, vol. 331, no. 6018, pp. 717–719, Sept 2007.

[2] A. Goldsmith, *Wireless Communications*, Cambridge University Press, Cambridge, MA, 2006.

[3] I. E. Telatar, "Capacity of Multi-antenna Gaussian Channels," *European Transactions on Telecommunications*, vol. 10, no. 6, pp. 585–595, 1999.

[4] Z. Pi and F. Khan, "An Introduction to Millimeter-Wave Mobile Broadband Systems," *IEEE Comm. Mag.*, vol. 49, no. 6, pp. 101–107, June 2011.

[5] J. Brady, N. Behdad, and A.M. Sayeed, "Beamspace MIMO for Millimeter-Wave Communications: System Architecture, Modeling, Analysis, and Measurements," *Antennas and Propagation, IEEE Transactions on*, vol. 61, no. 7, pp. 3814–3827, July 2013.

[6] A. M. Sayeed and N. Behdad, "Continuous Aperture Phased MIMO: Basic Theory and Applications," in *Proc. Allerton Conference*, Sept. 29-Oct. 1 2010, pp. 1196 –1203.

[7] Akbar M. Sayeed and Nader Behdad, "Continuous Aperture Phased MIMO: A new architecture for optimum line-of-sight links," in *Proc. 2011 IEEE Antennas and Propagation Sysmposium*, July 2011, pp. 293–296.

[8] D. Tse and P. Viswanath, *Fundamentals of Wireless Communication*, Cambridge University Press, Cambridge, MA, 2005.

[9] A. M. Sayeed, "Deconstructing Multiantenna Fading Channels," *IEEE Trans. Signal Processsing*, vol. 50, no. 10, pp. 2563–2579, Oct. 2002.

[10] R. J. Mailloux, *Phased Array Antenna Handbook*, Artech House, 2nd edition, 2005.

[11] T. S. Rappaport, E. Ben-Dor, J. N. Murdock, and Y. Qiao, "38 GHz and 60 GHz Angle-dependent Propagation for Cellular & Peer-to-Peer Wireless Communications," in *IEEE International Conference on Communications (ICC)*, June 2012.

[12] Gi Hong Song, J. Brady, and A. Sayeed, "Beamspace mimo transceivers for low-complexity and near-optimal communication at mm-wave frequencies," in *Acoustics, Speech and Signal Processing (ICASSP), 2013 IEEE International Conference on*, May 2013, pp. 4394–4398.

[13] M. Moeneclaey and T. Batsele, "Carrier-independent NDA symbol synchronization for M-PSK, operating at only one sample per symbol," in *GLOBECOM '90.*, Dec 1990, pp. 594–598 vol.1.